MDPI

*Article*

# Facile Modification of Flexible Electrodes via Laser Transfer

Florin Andrei, Iulian Boerasu [ID], Mihaela Filipescu [ID] and Alexandra Palla-Papavlu *[ID]

Lasers Department, National Institute for Lasers, Plasma and Radiation Physics, Atomistilor 409,
077125 Magurele, Romania; florin.andrei@inflpr.ro (F.A.); iulian.boerasu@inflpr.ro (I.B.);
mihaela.filipescu@inflpr.ro (M.F.)
* Correspondence: alexandra.papavlu@inflpr.ro

**Abstract:** In this work, we report the modification of commercially available electrochemical electrodes with tin oxide ($SnO_2$) and Pd doped $SnO_2$ (Pd-$SnO_2$) via pulsed laser-induced forward transfer (LIFT). The pulsed light irradiation working as in situ pulsed photo-thermal treatment allows for the transfer of $SnO_2$ and Pd-$SnO_2$ from UV absorbing metal complex precursors onto flexible, commercially available screen-printed electrodes. The laser transfer conditions are optimized and the material transferred under different conditions is evaluated morphologically and chemically, and its functionality is tested against the detection of copper ions. For example, by applying laser fluences in the range 100–250 mJ/cm$^2$, the shape and the size of the transferred features ranges from nano-polyhedrons to near corner-grown cubic Pd-$SnO_2$ or near cubic Pd-$SnO_2$. In addition, the EDX analysis is consistent with the XPS findings, i.e., following laser transfer, Pd amounts lower than 0.5% are present in the Pd-$SnO_2$ pixels. First sensing tests were carried out and the transferred Pd-$SnO_2$ proved to enhance the cathodic peak when exposed to Cu(II) ions. This photo-initiated fabrication technology opens a promising way for the low-cost and high-throughput manufacturing of metal oxides as well as for electrodes for heavy metal ion detection.

**Keywords:** $SnO_2$; Pd-$SnO_2$; laser transfer; LIFT; electrodes; acetylacetonates

## 1. Introduction

Metal acetylacetonates are compounds derived from the acetylacetonate anion and metal ions [1] and they are currently utilized in a plethora of applications, such as precursors for catalysis [2], for the development of hybrid nanomaterials or membranes with enhanced gas separation performance [3], in energy storage applications [4,5], in sensor designs [6,7], in oxygen reduction reaction [8,9] or in generation of hydrogen [10].

Recently, numerous studies dedicated to the film-forming capacity of metal acetylacetonates have been reported, as these films are particularly attractive in optoelectronic applications [11,12] or as corrosion resistant coatings [13]. In addition, films of $ZrO_2$, $HfO_2$, $SnO_2$, etc., prepared from metal acetylacetonate solutions, are particularly appealing due to the low deposition temperatures which make them suitable for being applied to flexible substrates and with a good potential for scaling up [14–16].

Although there are numerous deposition methods for metal oxide thin films from metal acetylacetonates, such as metal organic chemical vapor deposition technique [17], metal organic coating photolysis process [18], combined reactive magnetron sputtering and plasma decomposition [19], the laser-based methods have been proven as excellent alternatives.

Laser-induced forward transfer (LIFT) is a simple process, where a pulsed laser beam is focused through a transparent substrate (i.e., donor substrate) onto a thin layer (donor layer) [20–23]. Each laser pulse allows the precise and well localized transfer of the donor layer as a pixel (with different shapes, areas and thicknesses) on a rigid or flexible substrate (receiver substrate) that is placed parallel, in contact to or at short distance from the donor. One of the advantages of LIFT is that it allows the transfer of materials in different phases

(liquid [20,24–26] or solid [27–31]) with high resolution and without contamination, even if the process is carried out in air. This technique can be successfully applied for processing of sensors [31], organic light emitting diodes [32], flip-chip devices [33], etc. Recently, LIFT was used as method of bactericidal treatment of pathogenic bacterial biofilms in vitro [34]. In the work of Soulis et al. [35], a biosensor for the detection of organophosphorous and carbamate pesticides has been reported, which is based on LIFT of different liquid mixtures, i.e., chitosan, acetylcholinesterase, carbon black applied to modify the surface of the SPE electrodes.

Furthermore, in [36,37], an approach based on laser-induced forward transfer, i.e., reactive LIFT (rLIFT), has been used to transfer $SnO_2$ pixels from $SnCl_2(acac)_2$ precursors. The main advantage of the rLIFT method is related to the low decomposition temperatures of the acetylacetonates combined with the spatial resolution of the LIFT technique. Later on, in a study conducted by A. Palla-Papavlu et al. [38], the rLIFT technique was used for the integration of $SnO_2$ and $Pd-SnO_2$ in micro-sensors. Starting from a metal precursor, the rLIFT allows the conversion into the corresponding metal oxide as a result of the photochemical and thermal processes. This can be considered as an important advantage as the fabrication process is shorted. It was proven that the rLIFT fabricated sensors based on tin oxide had up to 4 times higher sensitivities than the commercial sensors (with $SnO_2$ inkjet printed). In addition, the sensitivity to $CH_4$ of the sensors based on $Pd-SnO_2$ is significantly increased in comparison with the pure $SnO_2$ sensors.

Therefore, due to our continued interest in the development of sensors by applying LIFT and modifications of LIFT, in this work, we have transferred different $SnO_2$ and $Pd-SnO_2$ pixels onto flexible and low-cost electrochemical sensors and tested them for their ability to detect Cu ions. We have chosen $Pd-SnO_2$ due to the fact that noble metal additives are frequently used to improve the performance of metal oxide gas sensors [39]. The novelty of the paper is twofold: on one hand, we focus on the promotion of LIFT as a viable method to decorate electrodes for sensors, and, on the other hand, we aim at improving and developing new flexible sensors by a low-cost, solvent free, environmentally friendly method.

## 2. Materials and Methods

### 2.1. Preparation of the Donor Substrates

$SnCl_2(acac)_2$ (from Merck KGaA, Darmstadt, Germany) is synthesized according to the procedure described in [36–38]. $SnCl_2$ is mixed with acetylacetone and HCl. One wt% Triton X-100 (from Merck KGaA, Darmstadt, Germany) is added to the final solution in order to improve the wettability when spin coating on the quartz substrates. The solution is filtered with a 1 μm filter and spin coated at 2500 rpm, resulting in thin films with a thickness of approximately 900 nm ± 70 nm.

A commercially available Pd metal precursor solution (i.e., $Pd(acac)_2$) is purchased from Merck KGaA, Darmstadt, Germany and 0.5 wt% of $Pd(acac)_2$ is added to the $SnCl_2(acac)_2$ solution applied for spin coating.

### 2.2. Electrode Modification via Laser-Induced Forward Transfer

Flexible and low-cost SPPEDOTEs (Dropsense ref. P10, Asturias, Spain) with carbon counter electrode (CE), reference electrode (RE) made of silver and working electrode (WE) based on [poly(3,4 ethylenedioxythiophene)] (PEDOT) are used as receiver substrates. The WE consisting of 4 mm diameter PEDOT disk of identical commercial screen-printed electrode (SPE) is modified with $SnO_2$ and $Pd-SnO_2$ using an in-house laser-induced forward transfer (LIFT) system.

The LIFT setup (the sketch is shown in Figure 1) used in this work consists of a pulsed ArF laser (193 nm emission wavelength, 20 ns pulse length, 1 Hz repetition rate, from Coherent Inc., Santa Clara, CA, USA) which is guided and imaged with an optical system at the quartz substrate–$SnCl_2(acac)_2$ layer interface and as a result of the rapid increase in pressure at the quartz-$SnCl_2(acac)_2$ interface, a part of the donor layer is transferred

(further named pixel) onto the receiving substrate. A computer-controlled xyz translation stage allows the displacement of both donor and receiving substrates with respect to the laser beam. The donor and receiver are placed parallel and in close proximity (<10 μm). All experiments are carried out under ambient pressure at temperatures close to room temperature. The laser fluence is varied over a broad range, i.e., from 100 to 250 mJ/cm$^2$.
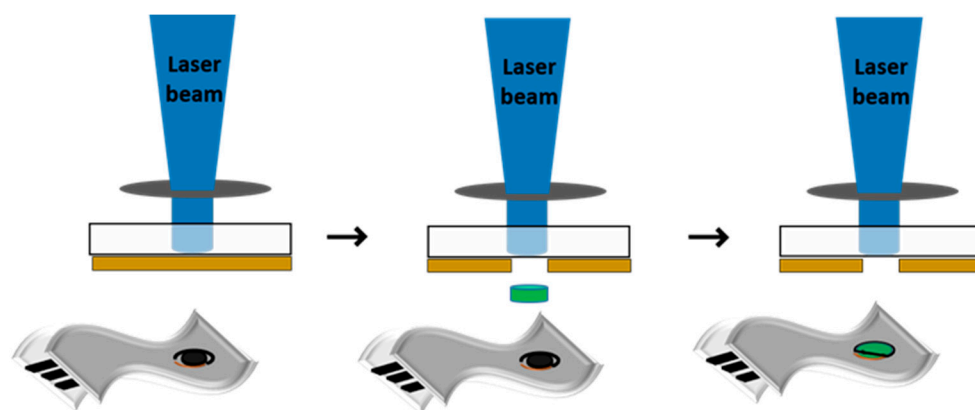


**Figure 1.** Scheme of the LIFT process for printing $SnO_2$ and $Pd-SnO_2$ pixels from $SnCl_2(acac)_2$ and $Pd-SnO_2$ donors onto flexible electrochemical electrodes.

### 2.3. Investigation of Electrode Functionality

All chemicals are analytical grade and are used with no further purification. Anhydrous copper sulphate ($CuSO_4$; purity $\geq$ 99.99%) is purchased from Merck KGaA, Darmstadt, Germany. For the preparation of acetate buffer solution, glacial acetic acid and sodium acetate (both from Merck KGaA Darmstadt, Germany) are acquired.

The electrochemical investigations are carried out with an AutoLab PGSTAT302N (Utrecht, The Netherlands) controlled by NOVA version 1.11 software (Utrecht, The Netherlands). The connection between the potentiostat and electrodes is made using a standard cable connector for screen-printed electrodes. All the sensors are tested for copper detection by cyclic voltammetry measurements scanning the potential from −1.4 V to 0.4 V and reversely using a scan rate of 100 mV/s. An amount of 100 ppm of $Cu^{2+}$ is added to 0.1 M acetate buffer solution (pH = 5.0 upH) and is energetically stirred with for 20 min.

### 2.4. Surface Investigation of the Transferred Material and Functionalized Electrodes

The transferred $SnO_2$ and $Pd-SnO_2$ pixels as well as the donor films prior to ablation are investigated by optical microscopy. The images are acquired with an Olympus SZH 10 Research Stereo microscope (Olympus CO (Europa) GMBH, Hamburg, Germany) coupled with a Stingray F145C CCD camera (Stadtroda, Germany).

Atomic force microscopy (AFM) (XE 100 from Park System, Suwon, Korea) measurements are carried out to analyze the surface roughness of the spin coated $SnCl_2(acac)_2$ and $Pd-SnCl_2(acac)_2$ donor films and $SnO_2$, respectively, $Pd-SnO_2$ transferred pixels on different areas and dimensions (40 × 40 μm$^2$ and 5 × 5 μm$^2$). All AFM images are obtained at ambient conditions. Commercial silicon cantilevers are used (OMCL-AC240TS, Olympus cantilevers) with 70 kHz nominal resonance frequency and 2 N/m nominal force constant.

The surface morphology and chemical composition of both $SnCl_2(acac)_2$ donors and transferred pixels features are examined by scanning electron microscopy (SEM) and energy-dispersive spectroscopy (EDS). These investigations are achieved by using an Apreo FEG High-Resolution Scanning Electron Microscope (HR-SEM), model S LoVac (Thermo Fisher Scientific Inc., Hillsboro, OR, USA) equipped with a Trinity detector system and coupled with an EDAX Trident (EDS-EBSD-WDS) Analysis System (AMETEK Inc., Mahwah, NJ, USA). To assist with simultaneous surface imaging and composition analysis, the involved Apreo S LoVac HR-SEM is operated in High-Vacuum mode at the analytical working distance (10 mm) with 10 kV voltage electron beams and 25 pA beam currents.

To completely avoid the charge mitigation issue, a thin layer of gold (Au) (5 nm thick) is sputtered on the samples.

The chemical states of Pd and Sn in the transferred pixels are analyzed by x-ray photoelectron spectroscopy (XPS). The XPS spectra are recorded using a ESCALAB Xi+ system from Thermo Fisher Scientific (Waltham, MA, USA). XPS survey spectra and high-resolution XPS scan spectra are acquired for the $SnO_2$ and $Pd-SnO_2$ pixels. The survey scans are acquired using Al K$\alpha$ gun, with spot size 900 μm, pass energy of 50.0 eV, energy step size 1.00 eV, and five scans are accumulated, while for the high-resolution XPS spectra, the pass energy is set to 20.0 eV, and energy step size is 0.10 eV and 35 scans are accumulated. The pressure during the acquisition of the spectra is $5 \times 10^{-9}$ mbar.

Contact-angle measurements are carried out with a KSV CAM101 microscope (from KSV Instruments Ltd., Helsinki, Finland) equipped with a video camera. All contact-angle measurements are obtained by applying the sessile drop method, i.e., a syringe is used which disperses double-distilled water droplets with a volume of $1 \pm 0.1$ μL. Five different points are measured for every pixel deposited onto the commercial electrodes, and the contact angle reported is the average of these measurements.

## 3. Results and Discussion

### 3.1. Morphological Investigation

The aim of this study is to get insight into the possibility to use $SnO_2$ and $Pd-SnO_2$ pixels printed from metal acetylacetonates for the development of flexible electrodes which can detect Cu(II) ions. Therefore, a systematic investigation of the surface of $SnO_2$ and $Pd-SnO_2$ printed pixels is carried out first.

In order to print the $SnO_2$ and $Pd-SnO_2$ pixels, reproducible donor films from $SnCl_2(acac)_2$ and $Pd(acac)_2$ precursors are fabricated. Two types of donors based on $SnCl_2(acac)_2$ are fabricated, which have distinctive morphologies: (i) "wrinkle"-like structures with predominant valleys (Rsk = −1.105) that induce a high roughness (Rq = 156.17 nm) of the $SnCl_2(acac)_2$ thin layer (Figure 2a) and (ii) a relatively flat surface with an almost symmetrical height distribution (as indicated by the Rsk value close to zero), with lower roughness (Rq = 97.25 nm) and with valleys, as revealed by the negative value of Rsk (−0.379) that characterize the $Pd-SnCl_2(acac)_2$ donor surface. On a large area (40 μm × 40 μm), the surface of this donor has pores with different sizes (0.3–2.5 μm) (Figure 2b).



(a)



(b)
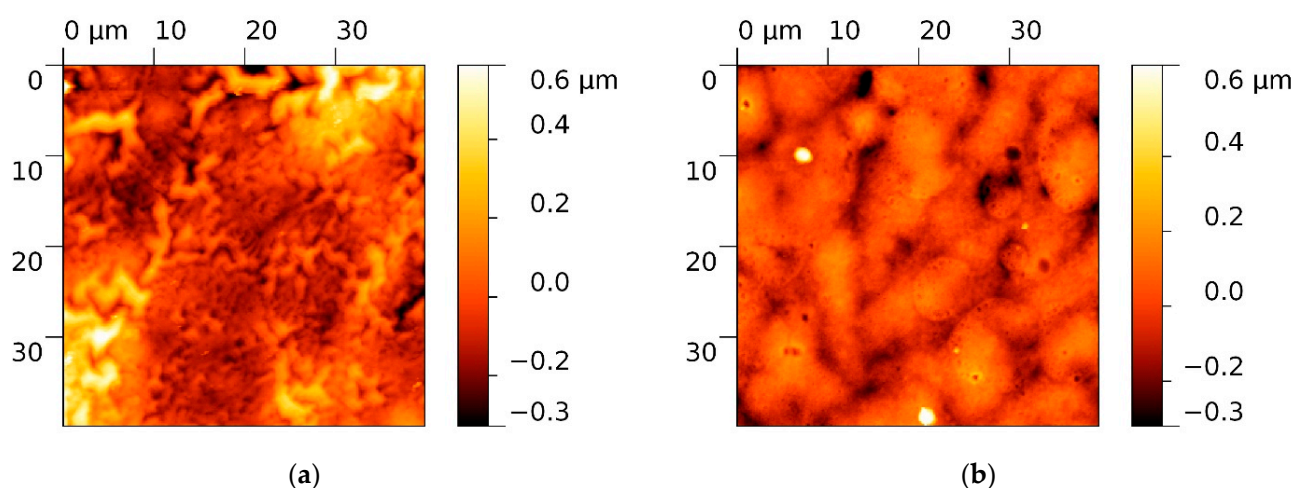
**Figure 2.** AFM images of the (**a**) $SnCl_2(acac)_2$ donor surface, (**b**) $Pd-SnCl_2(acac)_2$ donor surface.

The parameters describing the surface morphology (Rq, Min, Max, Rsk), as extracted from AFM scans, are collected in Table 1. The average squared roughness value (Rq) represents the standard deviation of the height value in the selected region, Min is the minimum height value of the scanned region and Max is the maximum height value of the region. Another important parameter that can be extracted from AFM investigation

is the skewness (Rsk). Skewness is used to measure the profile symmetry about mean line. When the height distribution is symmetrical, Rsk is zero. If the height distribution is asymmetrical, and the surface has more peaks than valleys, the skewness moment is positive, and if the surface is more planar and valleys are predominant, the Rsk is negative.

**Table 1.** AFM parameters that describe the surface morphology for (40 μm × 40 μm) scanned areas.

| Donor | Min (nm) | Max (nm) | Rq (nm) | Rsk | Thickness (nm) |
|---|---|---|---|---|---|
| $SnCl_2(acac)_2$ | −457.323 | 781.542 | 156.176 | −1.105 | 1085 |
| $Pd\text{-}SnCl_2(acac)_2$ | −519.386 | 781.174 | 97.251 | −0.379 | 895 |

Once reproducible donors are obtained, laser-induced forward transfer is applied to transfer $SnO_2$ and $Pd\text{-}SnO_2$ pixels onto glass substrates. The fluence is varied over a broad range, i.e., from conditions insufficient to break the donor layer to high irradiation fluences (250 mJ/cm$^2$), in order to optimize the shape of the transferred pixels. The threshold fluence for the complete removal and transfer of either $SnO_2$ or $Pd\text{-}SnO_2$ thin films from the irradiated area (250 μm in diameter spot) is 100 mJ/cm$^2$. All transferred pixels have a circular shape, are regularly arranged, and in some cases, the edges are less uniform, e.g., the pixels at 200 and 250 mJ/cm$^2$ have a negligible amount of material scattered outside the pixel area. We found that the transfer of $Pd\text{-}SnO_2$ pixels occurs for the same conditions as for $SnO_2$. An example of optical micrographs of the $Pd\text{-}SnO_2$ pixels obtained immediately after transfer at different laser fluences are displayed in Figure 3.
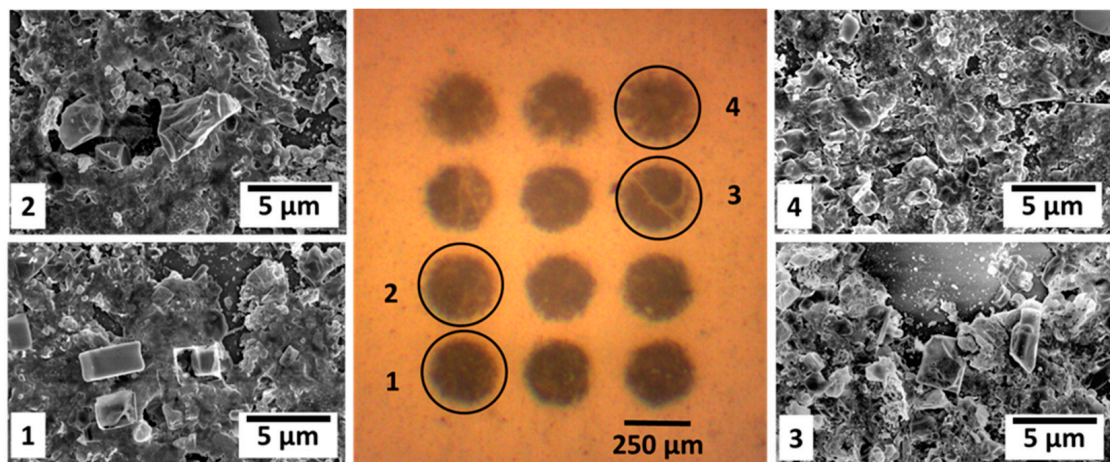


**Figure 3.** (Center image) Optical microscopy image of a $Pd\text{-}SnO_2$ pixel array obtained by varying the laser fluence between 100 mJ/cm$^2$ (lowest row) and 250 mJ/cm$^2$ (top row). Images 1–4 represent scanning electron microscopy images taken in the middle of the $Pd\text{-}SnO_2$ pixel transferred at: image 1—100 mJ/cm$^2$; image 2—150 mJ/cm$^2$; image 3—200 mJ/cm$^2$; and image 4—250 mJ/cm$^2$.

An in-depth investigation of the topography is carried out by SEM, which reveals that the distribution of material inside the pixel area is dependent on the laser fluence. The shape and size of the features observed inside the pixel range from nano-polyhedrons, to near corner-grown cubic $Pd\text{-}SnO_2$, or near cubic $Pd\text{-}SnO_2$. The high magnification micrographs recorded on the selected pixels, marked 1–4 in Figure 3, reveal the surface morphology and topography of the transferred layer, which was originally the bottom part of the $Pd\text{-}SnCl_2(acac)_2$ donor target. Although the transferred material covers the substrate, there are distinguishable visible voids on the pixels' surface. Noticeably, the number, shape and size of the distinguished voids varies from the pixel marked 1 to pixel 4. While the surface of pixel 1 appears to be coarse and includes a large amount of micro-porosity, the surface of pixel 2 is characterized by a smooth topography and visible macro-porosities. Furthermore, large size cavities are visible on the surfaces of pixel 3 and 4. Some crystalline aggregates

are visible on the surface of the transferred layer, as shown in Figure 3. Interestingly, both the density and size of the observed crystals seems to gradually increase from pixel 1 to pixel 4. Another finding in Figure 3 (pixel 3 & 4) is the coincidence of the cavity's shape and size with those of the observed crystals. According to this observation, it seems that the observed large cavities on the pixel 3 & 4 surfaces (dashed arrow) are formed by crystals pulled out (solid arrow) during the LIFT process.

Furthermore, $SnO_2$ and $Pd-SnO_2$ pixels have been transferred at 100 mJ/cm$^2$ laser fluence onto the commercially carbon electrodes in order to further test their functionality by typical cyclic voltammetry. An example of a transferred $SnO_2$ and $Pd-SnO_2$ pixel onto the surface of the working electrode is shown in Figure 4. Both the $SnO_2$ and $Pd-SnO_2$ transferred pixel morphology presents irregular grains with micrometric sizes (1–1.5 μm) and large agglomerations (>5 μm). The scanned surface is relatively planar with an almost symmetrical height distribution (Rsk value close to zero), with high roughness (Rq = 412 nm) and valleys (revealed by the negative value of Rsk).
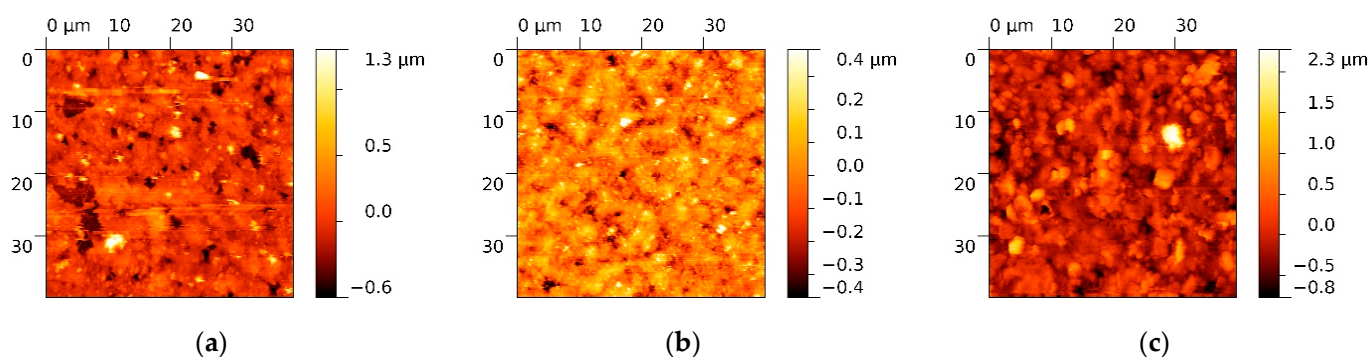


**Figure 4.** AFM images of (**a**) clean surface of the working electrode, (**b**) $SnO_2$ pixel transferred at 100 mJ/cm$^2$ laser fluence on the surface of the working electrode, and (**c**) $Pd-SnO_2$ pixel transferred at 100 mJ/cm$^2$ laser fluence on the surface of the working electrode.

The differences between the surface morphology of the donor layers (i.e., $SnCl_2(acac)_2$ and $Pd-SnCl_2(acac)_2$) and the surface morphology of the transferred material appear due to the transformation of the metal precursor to $SnO_2$ and $Pd-SnO_2$ during laser transfer as a result of the photochemical and thermal processes.

### 3.2. Chemical Investigation

The scope of this study is to demonstrate the fabrication of a proof-of-concept system where commercially available electrodes are decorated with thin film pixels by rLIFT technique. In this section, we aim at describing the chemical states of Pd and Sn from the transferred $SnO_2$ and $Pd-SnO_2$ pixels in order to provide more chemical information for improving the sensitivity of the sensor.

First, in order to assess any modification in the elemental composition by the transfer process, a set of EDX analyses are carried out on the selected pixels from Figure 3. The EDX spectra recorded on pixel 1, which is similar, in terms of detected elements, to the spectra belonging to pixels 2–4, is shown in Figure 5.
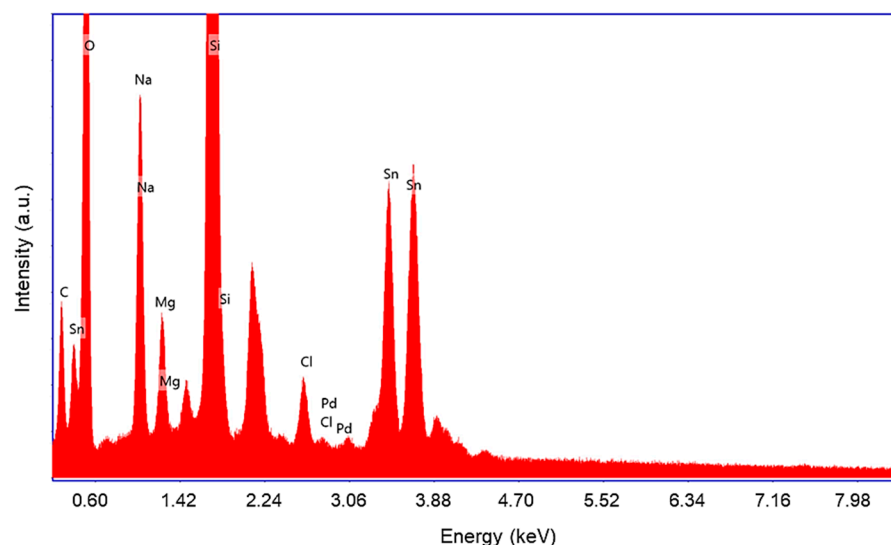
**Figure 5.** Typical EDX spectra recorded on the transferred Pd-SnO$_2$ pixels.

The EDX analysis reveals that the transferred material consists of O, Sn and Pd elements. However, there were also detected Na, K, Mg and Cl elements as originated from the target donor synthesis process. The detected Si is, of course, attributed to glass used as pixel substrate. The C peak in EDX spectra is due to some C cross-contamination during the sample handling process. The EDX spectra includes two non-labelled visible peaks. The first of them, located at 2.3 keV, is attributed to Au used as charge mitigation element for SEM analysis. The other one, located at 1.48 keV, is attributed to the Al sample-holder.

The entire acquired EDX spectra are software processed (TEAM software, AMETEK-EDAX Inc., Mahwah, NJ, USA) utilizing the eZAF algorithm for standardless quantitative analysis of Pd, Sn and O elements in the transferred pixels 1–4. The results obtained are shown in Table 2. In the standardless quantitative process of element determination, all identified compositions are taken into account, but only the elements of interest are quantified (O, Pd and Sn) by resuming them to 100.

**Table 2.** EDX analysis using the standardless ZAF quantification method of Pd, Sn and O elements in the transferred pixels 1–4.

| Element | Pixel 1 | | | Pixel 2 | | | Pixel 3 | | | Pixel 4 | | |
| | wt % | Atomic % | Error % | wt % | Atomic % | Error % | wt % | Atomic % | Error % | wt % | Atomic % | Error % |
|---|---|---|---|---|---|---|---|---|---|---|---|---|
| OK | 51.34 | 88.67 | 4.29 | 46.92 | 88.77 | 4.52 | 40.09 | 83.23 | 4.82 | 41.88 | 84.23 | 4.89 |
| PdL | 0.04 | 0.01 | 17.45 | 0.07 | 0.02 | 15.91 | 0.26 | 0.08 | 10.00 | 0.39 | 0.12 | 11.87 |
| SnL | 48.62 | 11.32 | 3.04 | 53.02 | 13.22 | 2.89 | 59.65 | 16.69 | 2.67 | 57.73 | 15.65 | 2.68 |

The as computed results highlights that the Pd content is gradually increasing from pixel 1 to pixel 4.

As shown in Table 2, while the quantification error of O, an Sn element, is in the range of the standardless method, i.e., 3–10% [40], the quantification error of the Pd element is noticeably higher for pixel 1 and pixel 2. The origin of this increased error is, of course, related to the pixel 1 & 2 surfaces' roughness, as revealed through AFM and SEM analysis. Further on, XPS is used to analyze the chemical composition and the nature of the chemical bonds of both the SnO$_2$ and Pd-SnO$_2$ pixel surfaces. The XPS spectra of the SnO$_2$ and Pd-SnO$_2$ pixels together with the atomic concentrations (shown in Table 3) of the SnO$_2$ pixels

transferred by LIFT at 100 mJ/cm$^2$ laser fluence is shown in Figure 6a–c and Table 3, and is consistent with those reported elsewhere [41–43]. Spin–orbit doublet peaks at $\simeq$486 eV (Sn$^{2+}$ 3d$_{5/2}$) and $\simeq$495 eV (Sn$^{2+}$ 3d$_{3/2}$) can be observed in the Sn 3d spectra. As can be observed from Figure 6, the binding energies of both the Sn 3d$_{5/2}$ and Sn 3d$_{3/2}$ peaks for the SnO$_2$ and Pd-SnO$_2$ pixels have different values (i.e., 486.1 eV and 495.22 eV for SnO$_2$ and 486.49 eV and 494.97 eV for Pd-SnO$_2$). The trend of decreasing the binding energies of Sn 3d$_{5/2}$ (by $-0.3$ eV in our case) by doping Pd in SnO$_2$ has been reported earlier [43]. Although the mechanism has not been completely elucidated, the decrease in the Fermi level of the SnO$_2$ is attributed to the role of electronic sensitizer of the Pd. The same observation can be made for the O1s peak of SnO$_2$ as compared to the O1s peak of the Pd-SnO$_2$ pixel (i.e., 531.74 eV for SnO$_2$ and 531.3 eV for Pd-SnO$_2$). The O1s peak of both SnO$_2$ and Pd-SnO$_2$ pixels is asymmetric and exhibits an evident shoulder in the higher binding energy part, as shown in Figure 6b, which could be attributed to the oxygen atoms chemisorbed at the surface [42]. Furthermore, due to the fact that no Pd peak could be found at the surface of the Pd-SnO$_2$ pixels, we investigated the evolution of the O, C, Sn and Pd as a function of etching time, and our results are consistent with those from EDX, where an amount lower than 0.5% of Pd is present in the transferred pixels.



(a)



(b)



(c)
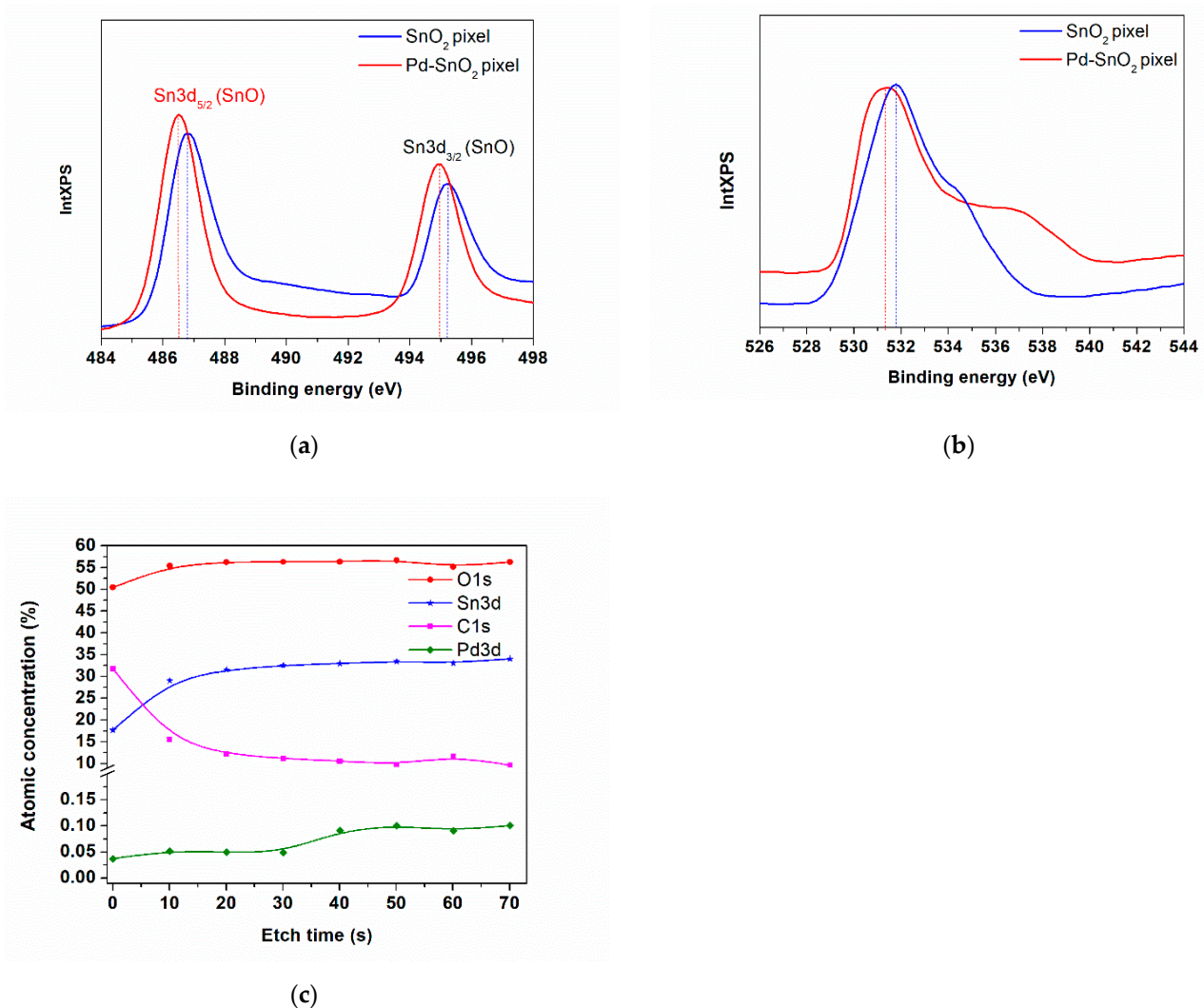
**Figure 6.** (**a**) Sn 3d, (**b**) O1s core-level XPS spectra of SnO$_2$ and Pd-SnO$_2$ pixels transferred at 100 mJ/cm$^2$; (**c**) Evolution of O, C, Sn and Pd as a function of etching time.

**Table 3.** Atomic concentrations (%) of $SnO_2$ pixels transferred by LIFT at 100 mJ/cm$^2$.

| Sn 3d$_5$ | O1s | C1s |
|---|---|---|
| 20.65 ± 2.5 | 66.3 ± 3.5 | 13.05 ± 4 |

Contact angle (CA) measurements are carried out to understand the surface wetting properties of the sensing electrode. The images of the water droplets on the uncoated, $SnO_2$ and Pd-$SnO_2$ coated sensors are shown in Figure 7.
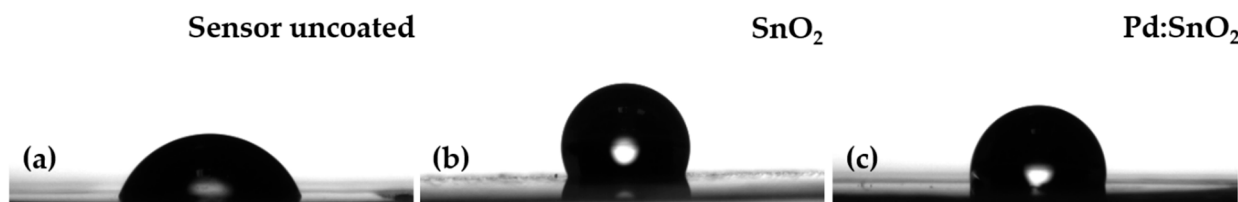


**Figure 7.** Contact angle images for (**a**) the uncoated working electrode, (**b**) the working electrode coated with a $SnO_2$ pixel and (**c**) the working electrode coated with a Pd-$SnO_2$ pixel.

The contact angle of the uncoated sensor is 69.75° ± 0.69°, whilst the contact angle for the $SnO_2$ coated sensor is 101.77° ± 0.24° and 95.4° ± 1.21° for Pd-$SnO_2$, respectively. The increase of the CA shows that the surface is more hydrophobic which is advantageous for self-cleaning of the sensor. Significantly, it demonstrates that the rLIFT results in a different surface wetting property, which is advantageous for any adsorption-based sensor development.

*3.3. Assessment of the LIFT Modified Electrodes Functionality*

A typical cyclic volammogram of 100 ppm $Cu^{2+}$ in 0.1 M acetate buffer solution (pH = 5.0 upH) obtained by using modified flexible screen-printed electrodes (SPE) based on PEDOT as working electrode is presented in Figure 8, the resulting data being presented in Table 4.
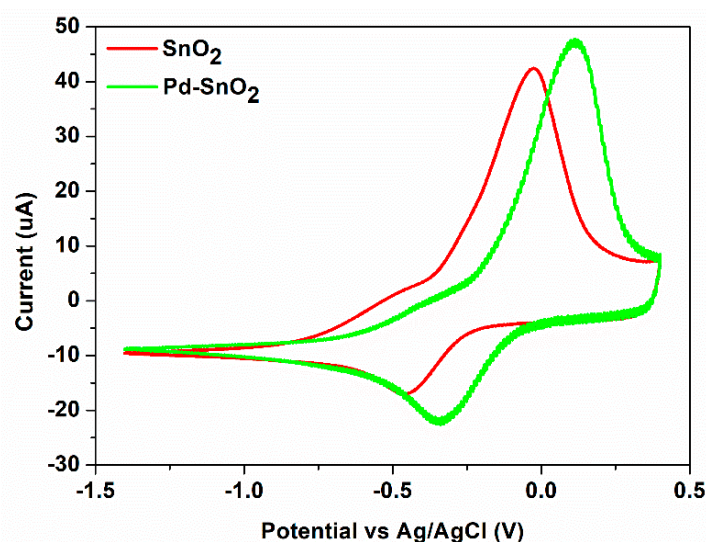


**Figure 8.** Cyclic voltammograms of $Cu^{2+}$ (100 ppm) in 0.1 M acetate buffer solution (pH = 5.0) recorded on red SPE-based $SnO_2$ and green SPE-based Pd-$SnO_2$.

**Table 4.** Data obtained from voltammograms recorded for $Cu^{2+}$ in acetate buffer on different $SnO_2$ and $Pd$-$SnO_2$ based sensors.

| Sensor | $Cu^{2+}$ Concentration | pH | Peak Current (µA) | | Peak Potential (mV) | | $\Delta Ep = Epa - Epc$ | \|ipa/ipc\| | Ref. |
|---|---|---|---|---|---|---|---|---|---|
| | | | (−) ipc | ipa | (−) Epc | Epa | | | |
| Commercial SPE-PEDOT | 100 ppm | 5 | 11.41 | 42.9 | 430 | 26 | 450 | 3.76 | - |
| GCE | ca. 188 ppm | 1.03 | 50.99 | 140.24 | 82 | 53 | 135 | 2.75 | [44] |
| GCE | ca. 135 ppm | 5.3 | 125 | 148.2 | 301.4 | 291.52 | 592.92 | 1.19 | [45] |
| Modified-SPCE | 1 ppm | 8 | - | <2 | - | - | - | - | [46] |
| $SnO_2$ | 100 ppm | 5 | 10.01 | 38.03 | 460 | −31 | 429 | 2.90 | This work |
| $Pd$-$SnO_2$ | 100 ppm | 5 | 15.18 | 44.06 | 340 | 110 | 450 | 3.79 | This work |

GCE—glassy carbon electrode; SPCE—screen-printed carbon electrode.

A single cathodic peak, $I_{pc}$ is obtained during the forward scan at in the range of $-476$ mV $\rightarrow -330$ mV, the $Cu^{2+}$ being reduced to $Cu^0$ by a two-electron transfer reaction ($Cu^{2+} + 2e^- \rightarrow Cu^0$). This is in good agreement with the study reported by Shaikh et. al., where they have demonstrated that bivalent copper is directly reduced to metallic copper in electrolyte solutions having pH > 4.08 [44]. In addition, the oxidation of copper ($Cu^0 \rightarrow Cu^{2+} + 2e^-$) is observed during the reverse, with an anodic peak at around +45 mV.

As can be observed in Table 4 the addition of $SnO_2$ to the commercial SPE leads to a small decrease of both anodic and cathodic peaks current. The peak potential separation ($\Delta E_p$) decreases to 429 mV, the sample showing a negative value of $-31$ mV for the anodic peak potential. The ratio between the current peaks is also lower (2.90) compared to the obtained value for the bare SPE. The addition of Pd nanoparticles to the $SnO_2$-SPE sensor leads to an increase of the currents, especially for the cathodic peak. This reveals that the addition of Pd to $SnO_2$ may provide the required conduction pathways at the surface of the electrode and ensures better electrochemical behavior. The peak potential separation is the same as that obtained for the commercial SPE and the current ratio is increased.

## 4. Conclusions

In this work, the combination of low-cost materials together with a facile and cost-efficient method to modify flexible electrodes for the detection of Cu ions has been evaluated. In particular, $SnO_2$ and $Pd$-$SnO_2$ thin film pixels were evaluated for their potential to amplify the signal of an electrochemical working electrode. Both the $SnO_2$ and $Pd$-$SnO_2$ thin film pixels were obtained by laser-induced forward transfer (LIFT) from metal acetylacetonates precursors which are decomposed under UV light. Extensive evaluation of the morphological and chemical properties of the transferred materials reveals that LIFT was successfully applied to obtain chemically stable $SnO_2$ and $Pd$-$SnO_2$ pixels which exhibit a high roughness. In addition, the contact angle measurements carried out onto the transferred $SnO_2$ and $Pd$-$SnO_2$ pixels highlight the possibility to tune the wettability of the screen-printed electrodes (SPE) by LIFT.

Finally, compared to the bare screen-printed electrodes, the addition of Pd nanoparticles to the $SnO_2$-SPE sensor, leads to an increase of the currents, especially for the cathodic peak. Thus, the LIFT fabricated $Pd$-$SnO_2$ electrodes could be used as a classic sensor for Cu ions detection. This result also suggests that this simple method could be used for decoration and modification of electrodes for the detection of other toxic ions.

## References

1.  Sodhi, R.K.; Paul, S. An Overview of Metal Acetylacetonates: Developing Areas/Routes to New Materials and Applications in Organic Syntheses. *Catal. Surv. Asia* **2018**, *22*, 31–62. [CrossRef]
2.  Caille, J.-R.; Debuigne, A.; Jérôme, R. Quinone Transfer Radical Polymerization (QTRP) of Styrene: Catalysis by Different Metal Complexes. *J. Polym. Sci. Part A Polym. Chem.* **2005**, *43*, 2723–2733. [CrossRef]
3.  Chua, M.L.; Xiao, Y.; Chung, T.S. Using Iron (III) Acetylacetonate as Both a Cross-Linker and Micropore Former to Develop Polyimide Membranes with Enhanced Gas Separation Performance. *Sep. Purif. Technol.* **2014**, *133*, 120–128. [CrossRef]
4.  Kucharyson, J.F.; Cheng, L.; Tung, S.O.; Curtiss, L.A.; Thompson, L.T. Predicting the Potentials, Solubilities and Stabilities of Metal-Acetylacetonates for Non-Aqueous Redox Flow Batteries Using Density Functional Theory Calculations. *J. Mater. Chem. A* **2017**, *5*, 13700–13709. [CrossRef]
5.  Kaneko, T.; Watanuki, Y.; Toyama, T.; Kojima, Y.; Nishimiya, N. Characterization and Hydrogen Sorption Behaviors of FeNiCr-Carbon Composites Derived from Fe, Ni and Cr-Containing Polyacrylonitrile Fibers Prepared by Electrospinning Method. *Int. J. Hydrogen Energy* **2017**, *42*, 10014–10022. [CrossRef]
6.  Inagaki, N.; Tasaka, S.; Nozue, Y. Plasma Polymerization of Metal Acetylacetonates and Application for Gas Sensor Devices. *J. Appl. Polym. Sci.* **1992**, *45*, 1041–1048. [CrossRef]
7.  Goncharov, T.; Nasriddinov, A.; Zubenko, A.; Tokarev, S.; Shatalova, T.; Khmelevsky, N.; Fedorova, O.; Rumyantseva, M. Nanocrystalline $SnO_2$ Functionalized with Ag(I) Organometallic Complexes as Materials for Low Temperature $H_2S$ Detection. *Materials* **2021**, *14*, 7778. [CrossRef]
8.  Kamedulski, P.; Skorupska, M.; Binkowski, P.; Arendarska, W.; Ilnicka, A.; Lukaszewicz, J.P. High surface area micro-mesoporous graphene for electrochemical applications. *Sci. Rep.* **2021**, *11*, 22054. [CrossRef]
9.  Vasiliev, V.P.; Manzhos, R.A.; Kochergin, V.K.; Krivenko, A.G.; Kabachkov, E.N.; Kulikov, A.V.; Shulga, Y.M.; Gutsev, G.L. A Facile Synthesis of Noble-Metal-Free Catalyst Based on Nitrogen Doped Graphene Oxide for Oxygen Reduction Reaction. *Materials* **2022**, *15*, 821. [CrossRef]
10.  Alwin, E.; Kočí, K.; Wojcieszak, R.; Zieliński, M.; Edelmannová, M.; Pietrowski, M. Influence of High Temperature Synthesis on the Structure of Graphitic Carbon Nitride and Its Hydrogen Generation Ability. *Materials* **2020**, *13*, 2756. [CrossRef]
11.  Holder, E.; Langeveld, B.M.W.; Schubert, U.S. New Trends in the Use of Transition Metal-Ligand Complexes for Applications in Electroluminescent Devices. *Adv. Mater.* **2005**, *17*, 1109–1121. [CrossRef]
12.  El-Mahalawy, A.M. Structural and Optical Characteristics of Nickel Bis(Acetylacetonate) Thin Films as a Buffer Layer for Optoelectronic Applications. *Mater. Sci. Semicond. Process.* **2019**, *100*, 145–158. [CrossRef]
13.  Taheri, M.; Naderi, R.; Saremi, M.; Mahdavian, M. Development of an Ecofriendly Silane Sol-Gel Coating with Zinc Acetylaceto-nate Corrosion Inhibitor for Active Protection of Mild Steel in Sodium Chloride Solution. *J. Sol.-Gel. Sci. Technol.* **2017**, *81*, 154–166. [CrossRef]
14.  Ortiz, A.; Alonso, J.C.; Haro-Poniatowski, E. Spray Deposition and Characterization of Zirconium-Oxide Thin Films. *J. Electron. Mater.* **2005**, *34*, 150–155. [CrossRef]
15.  Chang, Q.; Zhang, N.; Liu, W.; Ye, Q.; Yu, Y.; Chen, X.; Li, C. Thermal Properties and Gas Decomposition Products of Hafnium(IV) Acetylacetonate. *Asian J. Chem.* **2010**, *22*, 1935–1938.
16.  Singhal, A.; Sanyal, B.; Tyagi, A.K. Tin Oxide Nanocrystals: Controllable Synthesis, Characterization, Optical Properties and Mechanistic Insights into the Formation Process. *RSC Adv.* **2011**, *1*, 903–910. [CrossRef]

17. Adedeji, A.V.; Egharevba, G.O.; Jeynes, C.; Ajayi, E.O.B. Preparation and Characterization of Pyrolytically Deposited (Co-V-O and Cr-V-O) Thin Films. *Thin Solid Films* **2002**, *402*, 49–54. [CrossRef]

18. Tsuchiya, T.; Watanabe, A.; Imai, Y.; Niino, H.; Yabe, A.; Yamaguchi, I.; Manabe, T.; Kumagai, T.; Mizuta, S. Preparation of Metal Oxide Thin Films Using Coating Photolysis Process with ArF Excimer Laser. In *Proceedings of the 1st International Symposium on Laser Precision Microfabrication*; Miyamoto, I., Sugioka, K., Sigmon, T.W., Eds.; Spie-Int Soc Optical Engineering: Bellingham, WA, USA, 2000; Volume 4088, pp. 311–314.

19. Gil-Rostra, J.; Yubero, F.; Ferrer, F.J.; González-Elipe, A.R. Combined Reactive Magnetron Sputtering and Plasma Decomposition of Non-Volatile Precursors to Grow Luminescent Thin Films. *Surf. Coat. Technol.* **2013**, *222*, 144–150. [CrossRef]

20. Arnold, C.B.; Serra, P.; Pique, A. Laser Direct-Write Techniques for Printing of Complex Materials. *MRS Bull.* **2007**, *32*, 23–31. [CrossRef]

21. Springer, M.; Dusing, J.; Koch, J.; Jaschke, P.; Kaierle, S.; Overmayer, L. Laser-Induced Forward Transfer as a Potential Alternative to Pick-and-Place technology when Assembling Semiconductor Components. *J. Laser Appl.* **2021**, *33*, 042030. [CrossRef]

22. Sammartino, C.; Sedghani Cohen, S.; Kotler, Z.; Eliaz, N. Direct Writing of High-Resolution, High-Quality Pure Metal Patterns on Smooth Transparent Substrates by Laser-induced Forward Transfer Followed by a Novel Laser Treatment. *Adv. Eng. Mater.* **2021**, *23*, 2100245. [CrossRef]

23. Wang, X.; Zheng, J.; Mei, X.; Xu, B.; Miao, J. Laser Fabrication of fully Printed Graphene Oxide Microsensor. *Opt. Lasers Eng.* **2021**, *140*, 106520. [CrossRef]

24. Delaporte, P.; Alloncle, A.-P. Laser-induced forward transfer: A high resolution additive manufacturing technology. *Opt. Laser Technol.* **2016**, *78*, 33–41. [CrossRef]

25. Serra, P.; Duocastella, M.; Fernández-Pradas, J.M.; Morenza, J.L. Liquids microprinting through laser-induced forward transfer. *Appl. Surf. Sci.* **2009**, *255*, 5342–5345. [CrossRef]

26. Palla-Papavlu, A.; Patrascioiu, A.; Di Pietrantonio, F.; Fernández-Pradas, J.-M.; Cannatà, D.; Benetti, M.; D'Auria, S.; Verona, E.; Serra, P. Preparation of surface acoustic wave odor sensors by laser-induced forward transfer. *Sens. Actuators B Chem.* **2014**, *192*, 369–377. [CrossRef]

27. Gorodesky, N.; Sedghani-Cohen, S.; Fogel, O.; Silber, A.; Tkachev, M.; Kotler, Z.; Zalevsky, Z. Improving Compactness of 3D Metallic Microstructures Printed by Laser-Induced Forward Transfer. *Crystals* **2021**, *11*, 291. [CrossRef]

28. Visser, C.W.; Pohl, R.; Sun, C.; Roemer, G.-W.; in 't Veld, B.H.; Lohse, D. Toward 3D Printing of Pure Metals by Laser-Induced Forward Transfer. *Adv. Mater.* **2015**, *27*, 4087–4092. [CrossRef]

29. Mills, B.; Heath, D.J.; Feinaeugle, M.; Eason, R.W. LIFT of Solid Films (Ceramics and Polymers). In *Laser Printing of Functional Materials*; John Wiley & Sons, Ltd.: Hoboken, NJ, USA, 2018; pp. 175–198, ISBN 978-3-527-80510-5.

30. Makrygianni, M.; Zacharatos, F.; Andritsos, K.; Theodorakos, I.; Reppas, D.; Oikonomidis, N.; Spandonidis, C.; Zergioti, I. Eco-Friendly Lead-Free Solder Paste Printing via Laser-Induced Forward Transfer for the Assembly of Ultra-Fine Pitch Electronic Components. *Materials* **2021**, *14*, 3353. [CrossRef]

31. Papazoglou, S.; Zergioti, I. Laser Induced Forward Transfer (LIFT) of Nano-Micro Patterns for Sensor Applications. *Microelectron. Eng.* **2017**, *182*, 25–34. [CrossRef]

32. Shaw Stewart, J.; Lippert, T.; Nagel, M.; Nüesch, F.; Wokaun, A. Red-Green-Blue Polymer Light-Emitting Diode Pixels Printed by Optimized Laser-Induced Forward Transfer. *Appl. Phys. Lett.* **2012**, *100*, 203303. [CrossRef]

33. Charipar, K.M.; Charipar, N.A.; Prestigiacomo, J.C.; Bingham, N.S.; Pique, A. Laser Printing of Flip-Chip Interconnects for High Frequency Applications. *J. Manuf. Process.* **2018**, *32*, 110–115. [CrossRef]

34. Nastulyavichus, A.; Tolordava, E.; Rudenko, A.; Zazymkina, D.; Shakhov, P.; Busleev, N.; Romanova, Y.; Ionin, A.; Kudryashov, S. In Vitro Destruction of Pathogenic Bacterial Biofilms by Bactericidal Metallic Nanoparticles via Laser-Induced Forward Transfer. *Nanomaterials* **2020**, *10*, 2259. [CrossRef] [PubMed]

35. Soulis, D.; Trigazi, M.; Tsekensis, G.; Chandrinou, C.; Klinakis, A.; Zergioti, I. Facile and Low-Cost SPE Modification Towards Ultra-Sensitive Organophosphorous and Carbamate Pesticide Detection in Olive Oil. *Molecules* **2020**, *25*, 4988. [CrossRef] [PubMed]

36. Mattle, T.; Shaw-Stewart, J.; Hintennach, A.; Schneider, C.W.; Lippert, T.; Wokaun, A. Shadowgraphic Investigations into the Laser-Induced Forward Transfer of Different SnO$_2$ Precursor Films. *Appl. Surf. Sci.* **2013**, *278*, 77–81. [CrossRef]

37. Mattle, T.; Hintennach, A.; Lippert, T.; Wokaun, A. Laser induced forward transfer of SnO$_2$ for sensing applications using different precursors systems. *Appl. Phys. A* **2013**, *110*, 309–316. [CrossRef]

38. Palla Papavlu, A.; Mattle, T.; Temmel, S.; Lehmann, U.; Hintennach, A.; Grisel, A.; Wokaun, A.; Lippert, T. Highly Sensitive SnO$_2$ Sensor via Reactive Laser-Induced Transfer. *Sci. Rep.* **2016**, *6*, 25144. [CrossRef]

39. Gschwend, P.M.; Schenk, F.M.; Gogos, A.; Pratsinis, S.E. Acetone Sensing and Catalytic Conversion by Pd-Loaded SnO$_2$. *Materials* **2021**, *14*, 5921. [CrossRef]

40. Labar, J.L. Standardless Quantitative Analysis by X-Ray Spectrometry. *Scanning Microsc.* **1993**, *1993*, 10.

41. Ansell, R.O.; Dickinson, T.; Povey, A.F.; Sherwood, P.M.A. Quantitative use of the angular variation technique in studies of tin by X-ray photoelectron spectroscopy. *J. Electron. Spectros. Relat. Phenom.* **1977**, *11*, 301–313. [CrossRef]

42. Szuber, J.; Czempik, G.; Larciprete, R.; Koziej, D.; Adamowicz, B. XPS study of the L-CVD deposited SnO$_2$ thin films exposed to oxygen and hydrogen. *Thin Solid Films* **2001**, *391*, 198–203. [CrossRef]

43. Cao, X.; Cao, L.; Yao, W.; Ye, X. Structural Characterization of Pd-doped SnO$_2$ Thin Films Using XPS. *Surf. Interface Anal.* **1996**, *24*, 662–666. [CrossRef]

44. Shaikh, A.A.; Firdaws, J.; Badrunnessa; Serajee, S.; Rahman, M.S.; Bakshi, P.K. Electrochemical Studies of the PH Dependence of Cu(II) Reduction in Aqueous Britton-Robinson Buffer Solution. *Int. J. Electrochem. Sci.* **2011**, *6*, 2333–2343.

45. Haque, F.; Rahman, M.S.; Ahmed, E.; Bakshi, P.; Shaikh, A. A Cyclic Voltammetric Study of the Redox Reaction of Cu(II) in Presence of Ascorbic Acid in Different PH Media. *Dhaka Univ. J. Sci.* **2013**, *61*, 161–166. [CrossRef]

46. Mei, C.J.; Yusof, N.A.; Ahmad, S.A.A. Electrochemical Determination of Lead & Copper Ions Using Thiolated Calix[4]Arene-Modified Screen-Printed Carbon Electrode. *Chemosensors* **2021**, *9*, 157. [CrossRef]